# Computational Design of Metal Oxides to Enhance the Wetting and Adhesion of Silver-based Brazes on Yttria-Stabilized-Zirconia

Thanaphong Phongpreecha, Jason D. Nicholas, Thomas R. Bieler, Yue Qi*
Chemical Engineering and Materials Science Department,
Michigan State University, East Lansing, MI 48824

## Abstract

Ag-CuO is a broadly used reactive air brazing (RAB) system for effectively bonding ceramics and metal interfaces, especially for sealing yttria-stabilized zirconia (YSZ) to metals in solid-oxide fuel cells (SOFCs). To understand the superior performance of this braze, density functional theory (DFT) calculations were employed to investigate two mechanisms that can potentially increase the work of adhesion ($W_{\mathrm{adh}}$) and hence reduce the wetting angle of Ag on YSZ. It was found while the formation of Ag–dissolved O clusters at the Ag-YSZ interface can promote wetting, a much greater wetting angle reduction comes from the formation of CuO interlayers between Ag and YSZ. Further, the $W_{\mathrm{adh}}$ of an Ag/CuO and CuO/YSZ interface was found to be significantly higher than that of an Ag/YSZ interface. Based on simulation obtained-insights into metal to oxide bond formation, a simple descriptor was developed to predict Ag/oxide interface energies, predict Ag/oxide $W_{\mathrm{adh}}$, and search for potential oxide interlayers capable of promoting the wetting and adhesion of Ag on YSZ. Many simple metal oxides (single cation) were examined, however their $W_{\mathrm{adh}}$ with Ag was less than that of an Ag/CuO interface. Expanding the search to multi-cation oxides led to several promising candidates, such as $CuAlO_2$, $CuGaO_2$, and $Cu_3TiO_4$; all of which are also stable in the reducing SOFC conditions. Depending upon their solubility in molten Ag, these newly-identified oxides could either be pre-applied as wetting promoting interlayers or directly incorporated into Ag to form new reactive air brazes.

**Keyword:** metal/oxides interface, adhesion, brazing, computational materials design

*Corresponding author: Email: yueqi@egr.msu.edu Phone: 517-4321243

## 1. INTRODUCTION

Adhesive metal/metal-oxide interface bonds are critical in a variety of applications including the formation of durable passivation coatings, oxide-supported catalysts, solders, and brazes [1]. For instance, silver-based brazes have been used to separate the fuel (i.e. anode) and oxidant (i.e. cathode) chambers in solid oxide fuel cells due to their superior toughness and gas impermeability compared to glass or mica seals [2–6]. In this application, sealing is accomplished by brazing a yttria-stabilized zirconia (YSZ) electrolyte layer to a stainless steel (SS) support. Unfortunately, wetting and adhesion problems of conventional silver or copper based brazes often result in braze joint manufacturing defects (pores) and as-produced joint failure at the braze-YSZ interface [7–9].

To help overcome the poor wetting and adhesion issues of Ag on YSZ, a technique called reactive air brazing (RAB) has recently been developed [10–12]. Reactive air brazing is performed in air, and the braze alloy is intentionally designed to contain minor elements (such as Cu) that oxidize during brazing to promote wetting and adhesion. In fact, the addition of as little as 4 wt% CuO reduces the wetting angle of Ag on YSZ from 110$^{\circ}$ to ~45$^{\circ}$ [2,13–15]. Further, the fact that brazing can be done in the air prevents mechanical and electrochemical degradation of the oxygen-partial-pressure-sensitive SOFC cathode materials during brazing [16–18]. Lastly, Ag-CuO reactive air brazes have also shown an ability to bond metals to a variety of oxides including alumina, lanthanum strontium cobalt iron oxide, etc. [19–23].

As depicted in Fig. 1, two mechanisms have been suggested to facilitate the wetting and adhesion of Ag–CuO reactive air brazes on oxide surfaces. In *Mechanism I*, the presence of oxygen dissolved in molten Ag is hypothesized to cause a 20$^{\circ}$-35$^{\circ}$ drop in Ag on oxide wetting angles when brazing is performed in the air instead of inert atmospheres [25]. (Note, unlike most molten metals

at elevated temperatures in air, Ag is thermodynamically more stable than AgO under brazing conditions [26], suggesting that wetting improvements via the formation of crystalline AgO are unlikely). In *Mechanism II*, CuO is hypothesized to improve wetting and adhesion by forming a CuO-rich phase between the Ag and YSZ [23].

In the first half of the present study, the primary objective is to use atomistic modeling to determine, without interference from other factors, the extent to which these two mechanisms occur. We consider this is the basic step toward materials design. To examine *Mechanism I*, *Ab Initio* Molecular Dynamics (AIMD) was used to track the evolution of dissolved $O_2$ in liquid Ag near the Ag(*l*)/YSZ interface in Section 3.1. In addition, $O_2$ was initially placed at the Ag(*l*) surface, the Ag(*l*)/YSZ interface, or the Ag(*l*) center to determine if the dissolved oxygen lowered the wetting angle by altering either the Ag liquid-vapor surface energy ($\gamma_{LV}$), the solid-liquid interfacial energy ($\gamma_{SL}$), or both. To examine *Mechanism II* and determine the effect of a CuO interlayer between Ag and YSZ, DFT simulations were performed in Section 3.2 to calculate the work of adhesion, $W_{adh}$, of the Ag/YSZ, Ag/CuO, and Ag/YSZ interfaces. Ag wetting angles were then calculated from the computed surface and interface energies. Previous DFT-based surface studies have laid essential groundwork on the surface structures of these materials. Combined DFT and thermodynamic calculations have identified the lowest energy facets for CuO to be the stoichiometric (111) for the entire O chemical potential region where CuO is stable [27,28]. For YSZ, which has a cubic $ZrO_2$ (c-$ZrO_2$) structure, the O-terminated-(111) surface was shown to be the most stable in the entire oxygen chemical potential range encountered in a SOFC [29,30]. This is in accordance with the experimental HRTEM images of Ni/YSZ interfaces [31]. The surface structure of 9%-Y-doped YSZ (111) [32–34], which is shown experimentally to be in cubic phase

at room temperature, has also been modeled via DFT and will be used as a basis for the present study [35].

In the second half of the present work (Section 3.3), the objective was to use the conclusion gained from previous sections (section 3.1 & 3.2) that *Mechanism II* is the dominant one to develop a simple descriptor to predict Ag/oxide interface energies, predict Ag/oxide $W_{adh}$, and search for new oxide interlayers capable of promoting the wetting and adhesion of Ag on YSZ, while maintaining stability in reducing environments. Although many theoretical and DFT studies have shown that for a given oxide surface, metals with lower *d*-band occupancy (particularly *bcc* metals) can induce higher metal-O charge transfer, and hence higher $W_{adh}$ [36–39], studies of the reverse relationship, *i.e.* identifying the oxides yielding a higher $W_{adh}$ on a given metal (such as Ag), are scarce [38,40]. New brazing materials with other oxides are needed because the reduction of CuO on the anode side of Ag/CuO SOFC braze joints (CuO is thermodynamically unstable in the water-hydrogen mixtures found under SOFC operation [26]) induces pores that mechanically weaken the joint and limit joint lifetimes [41–44].

## 2. METHODS

### 2.1 Geometry Optimization

All calculations in this study were performed using the plane wave DFT implemented in Vienna *Ab Initio* Simulation Package (VASP). The exchange correlations were treated with both the Local Density Approximation (LDA) and the Generalized Gradient Approximation (GGA) by the Purdew−Burke−Ernzerhorf (PBE) functional, for comparison [45,46]. Projector augmented wave (PAW) potentials were used to represent the effective electron-core interaction [47]. The electronic convergence was achieved self-consistently with a plane-wave cutoff energy of 500 eV.

The two convergence criteria were $10^{-5}$ eV for the total energy, and 0.03 eVÅ$^{-1}$ for forces during structural relaxation via conjugate gradient minimization. A Monkhorst-Pack grid with *k*-spacing kept below 0.04 Å$^{-1}$ was used for convergence within 1-2 meV/atom. The *k*-spacing results in (4×4×1), (2×9×1), and (2×3×1) *k*-point meshes for Ag/YSZ, Ag/CuO, and CuO/YSZ interface cell, respectively. Gaussian smearing was employed with a sigma of 0.02 to achieve less than 1 meV/atom contribution from entropy. A spin-polarized calculation was performed with dipole moment correction along the perpendicular direction of the slabs. For strongly correlated transitional metal oxide, on-site coulomb interaction as introduced by Dudarev ($+U_{eff}$) was employed [48]. The values of $U_{eff}$ were taken from previous studies that employed LDA functional. These were 3.20 [49], 4.30 [49], 2.80 [50], 5.00 [51], 6.00 [52], 7.50 [53], and 7.50 [53] eV for the transition metals in α-$Cr_2O_3$, α-$Fe_2O_3$, $Rh_2O_3$, NiO, c-$CeO_2$, CuO, and $Cu_2O$, respectively. In the case for GGA-PBE functional calculation of both CuO and $Cu_2O$, $U_{eff}$ of 8.50 eV was used [54]. The details of these oxides, including surface termination, lattice constants, and surface energies are tabulated in the supplemental materials (Table S1).

**2.2 Slab Models for Surfaces and Interfaces**

Slab models were constructed to compute surface energies. The surface orientation of each oxide used in this study was the lowest energy identified in the literature [See Supplement]. All the oxide surfaces were stoichiometric in this study except the delafossite oxides and $Cu_3TiO_4$, as detailed in Table S1. Particularly for the O-terminated (111) slab of YSZ, which adopts a cubic $ZrO_2$ structure at SOFC operating and brazing temperatures [55], the surface structure was taken from previous computational studies using $(Y_2O_3)_{0.09}(ZrO_2)_{0.91}$ with the most preferable sites for Y and oxygen vacancies ($V_O^{\bullet\bullet}$) identified [32,34]. Specifically, the $V_O^{\bullet\bullet}$ was found to be at the subsurface of the first YSZ multilayer with Y substituting for Zr at the second nearest neighbors

positions (2NN), in the first and second multilayers [32]. This is in agreement with experimental observation that Y tends to segregate to the surface [56,57]. The minimum number of layers in each slab was determined to give converged surface energy, $\gamma_{i\mathrm{V}}$, within ±0.02 J/m$^2$; six layers for both Ag and Ni slabs, whereas for certain oxides, such as $ZrO_2$, NiO, and CuO, three layers were sufficient, and oxides of corundum type usually required five layers, while $Cu_2O$ needed four.

As shown in Fig. 2, all interface simulations utilized, unless otherwise stated, a sandwich model where two metal slabs sandwiched an oxide slab and 16 Å of vacuum was used to preclude interactions of the top and bottom metal slabs due to periodicity. In the sandwich model, the number of oxide layers in the middle was a double of that from converged surface energy calculation. Using this setup, the interatomic distances in the interior of each slab retained bulk characteristics, eliminating the need for atomic position constraints. To match the metal/oxide lattices, the sandwich models were constructed using Virtual NanoLab to generate several interface configurations. All models were constructed with mismatch strains below 6% in all directions. The interfacial lattice mismatch strain was partitioned equally between adjoining slabs. The relative lateral positions of the metal slab on the oxide slab were varied to at least 3 positions in order to identify the most preferable position. All sandwich models were constructed to have at least inversion symmetry to ensure that the two interfaces were identical, less affected by the dipole moment, and that the interface energy, $\gamma_{12}$, was uniquely defined.

The average interface width ($\Delta d$) was defined as the z-distance between the averaged z-positions of the atoms in the first layer of each side of the interface. For YSZ and CuO, only oxygen atoms of the outermost layer were taken into account. For liquid Ag, only atoms within ±0.5 Å range from the bottom most atom were used to compute the average.

The work of adhesion of the system was defined and calculated using the equation:

$$W_{\mathrm{adh}} \equiv (\gamma_{1\mathrm{V}} + \gamma_{2\mathrm{V}}) - \gamma_{12} = (E_1 + E_2 - E_{12})/2A \quad \text{(Eqn. 1)}$$

where $\gamma_{i\mathrm{V}}$ is the surface energy of the slab $i$, $\gamma_{12}$ is the solid-solid interface energy, $E_{\mathrm{i}}$ is the calculated energy of the slab $i$, $E_{12}$ is the calculated total energy of the interface system with slab 1 and 2, and $A$ is the model interface area. Therefore, $W_{\mathrm{adh}}$ was computed based on the energy difference between a simulation cell with slab 1 and slab 2 far apart and where slab 1 and 2 shared an interface. Then, the interface energy was computed using the relationship $\gamma_{12} = \gamma_{1\mathrm{V}} + \gamma_{2\mathrm{V}} - W_{\mathrm{adh}}$.

The wetting angle corresponding to the $W_{\mathrm{adh}}$ was calculated based on Young's equation:

$$\cos(\theta_{\mathrm{cal}}) = \frac{\gamma_{\mathrm{SV,oxide}} - \gamma_{12}}{\gamma_{\mathrm{SV,metal}}} = \frac{W_{\mathrm{adh}}}{\gamma_{\mathrm{SV,metal}}} - 1 \quad \text{(Eqn. 2)}$$

where $\gamma_{\mathrm{SV,oxide}}$ is the solid oxide surface energy from DFT calculation reported in Table S1, $\gamma_{12}$ is the DFT calculated solid-solid interface energy from Eqn. 1, $\gamma_{\mathrm{SV,metal}}$ is the solid metal surface energy calculated by DFT listed in Table S1, and $\theta_{\mathrm{cal}}$ is the estimated contact angle. Except for one liquid Ag on YSZ interface calculation, all the other interfaces were solid-solid interfaces. It should be noted that although the absolute magnitude of the $\theta_{\mathrm{cal}}$ values obtained from the solid-solid interface calculations, instead of liquid-solid, may be overestimated due to the higher surface energy of a solid compared to its liquid [58], but the calculated trends in wettability are expected to hold at brazing temperatures.

### 2.3 *Ab Initio* Molecular Dynamics

*Ab-initio* molecular dynamics (AIMD) was used to determine the adsorption and wetting behavior of Ag(*l*), with and without dissolved oxygen, on YSZ. At a brazing temperature of 1000 $^{\circ}$C, the solubility of $O_2$ in Ag is 1.93 mL, which translates to approximately 2 atoms of oxygen per

200 Ag atoms [59]. Hence, in these AIMD simulations, the Ag(*l*)/YSZ system was modeled as a ~1 nm thick molten Ag layer containing two oxygen atoms (for a total of 102 atoms) supported on a YSZ slab three unit cells thick. The basal plane YSZ atoms were fixed in position, the YSZ had a surface area of 181.44 Å$^2$, and a vacuum gap of 13 Å was placed above the liquid surface in the initial structure. This initial structure corresponds to the experimentally measured density of 9.30 g/mL for Ag(*l*) at 1000 ˚C [60]. As shown in Fig. 3, three different initial structures were generated by inserting the two oxygen atoms at either the YSZ interface, within the bulk of the Ag(*l*), or at the free surface of the molten Ag. Although the dissolved oxygen concentration used here was double the experimentally observed amount due to computational limitations, the calculated energy trends with oxygen position should still be applicable to real-world systems.

Both the molten Ag and the Ag(*l*)/YSZ interfaces were initially relaxed using classical MD with a COMPASS force field (Ag = ag_m, O in Ag = o_ag, Y = y3o, Zr = zr4o, and O in YSZ = o2z) implemented in Material Studio [61,62]. The force field was previously shown to give a melting temperature of metal closer to first-principle calculations than embedded atom model (EAM) method [63]. The evolution of these initial structures was simulated by constant-temperature, constant-volume ensemble (NVT) AIMD using spin-polarized DFT calculations with GGA-PBE functional. The AIMD calculations were performed at the Γ-point *k*-point. The constant temperature was controlled at 1280K by the Nosé–Hoover thermostat and the integration time step is 1 fs for a total of 3 ps. The average energy for the $W_{\mathrm{adh}}$ calculation was then obtained by sampling and minimizing 3 frames from the last 0.5 ps of the AIMD run using (2 × 2 × 1) *k*-points.

## 3. RESULTS AND DISCUSSION

### 3.1 The Role of the Oxygen at the Ag(*l*)/YSZ interface during Brazing Process

AIMD was employed to investigate the energetics in Ag(*l*)/YSZ interface in order to examine the mechanism of dissolved $O_2$ in enhancing wettability, *i.e. Mechanism I* in Fig. 1. AIMD was first performed to investigate dissolved $O_2$ in bulk liquid Ag. Dissociation of $O_2$ into Ag–O clusters was promptly observed, where O atoms formed 2.2-2.3 Å bonds with the Ag atoms surrounding them. This bond length is 5~10% longer than the Ag-O bond length in crystalline $Ag_2O$ (2.08 Å in GGA-PBE relaxed structure), a reasonable increase for the liquid phase. Analysis of the system by pair radial distribution (RDF) shown in Fig. S2 revealed that the nearest Ag-Ag distance peak was ~2.8 Å, in accordance with experimental measurements of pure Ag in a reducing atmosphere at 1050°C [64]. This indicated that the dilute concentration of oxygen in the Ag did not significantly alter the bulk behavior of the Ag.

Figure 3 shows three possible sites for Ag–O clusters to be at, including in the bulk (a), at the surface of molten silver (b), or at the interface of liquid-Ag/YSZ (c). Although not the objective of the present work, oxygen vacancies in all these initial positions were observed to move around within the YSZ slab during the AIMD simulations. Figure 3a and 3b show that Ag with Ag-O clusters in the bulk of the Ag or placed at the Ag-free surface drifted away from the YSZ (yielding a GGA-calculated $W_{\mathrm{adh}} \sim 0$ J/m$^2$ that may be a low considering the fact that GGA tends to underestimate binding energies). In contrast, Fig. 3c shows that Ag with Ag-O clusters at the Ag(*l*)/YSZ interface remained attached to the YSZ with a GGA-calculated $W_{\mathrm{adh}} = 0.43 \pm 0.01$ J/m$^2$. The arrangement in Fig. 3c, denoted henceforth as {Ag(*l*)+2O}/YSZ, had a lower overall energy than those in Fig. 3a and 3b, indicating that changes in the Ag(*l*)/YSZ interface, and not changes in the Ag free surface energy, are responsible for the Ag wetting enhancements experimentally observed when switching from inert Ag/YSZ brazing atmospheres to air [7,10].

Without the dissolved $O_2$, the pure liquid Ag has an average $W_{adh}$ (on YSZ from GGA-PBE functional) of only 0.11±0.01 J/m$^2$, resulting in a contact angle of 149$^\circ$ (Table 1). This is consistent with experimental observations showing that liquid Ag does not wet YSZ [7]. Although the results from GGA may be overestimated, the trend and the relative change of the wetting angles are expected to be reliable as will be shown in the next section. As shown in Table 1, the {Ag(*l*)+2O}/YSZ wetting angle was 38$^o$ less than that for pure Ag(*l*)/YSZ, in agreement with a 30$^o$ drop observed experimentally [7,69] (Table 1 also shows that the binding energy underestimated by the GGA-PBE method resulted in wetting angle predictions that were ~25$^o$ higher than those observed experimentally). Figure 3c also shows that the two oxygen atoms originally dissolved in the Ag near the Ag/YSZ interface hopped into the YSZ substrate, filling two YSZ oxygen vacancies in the process. The resulting increase in the YSZ surface oxygen vacancy concentration likely contributed to the increased $W_{adh}$ by providing additional sites for Ag-O bonding across the interface. Together, these results confirm *Mechanism I* (the hypothesis that oxygen dissolved in molten Ag is responsible for the ~20$^\circ$-35$^\circ$ drop in Ag on oxide wetting angles when brazing is performed in air instead of inert atmospheres).

### 3.2 Enhancement of Interface Adhesion by CuO

Before studying these solid interfaces, the accuracy and reliability of the results were evaluated. A Ni/YSZ interface was employed because of abundant existing computations and detailed experimental results, in contrast to limited studies of Ag adhesion on YSZ or $ZrO_2$. Table 2 shows the surface energy, interface energy, and $W_{adh}$ from GGA and LDA functionals for Ni[$1\bar{1}0$](111)||YSZ[$1\bar{1}0$](111) interface shown in Fig. S3. The $W_{adh}$ agreed well with the experimentally measured values. In fact, the LDA-predicted $W_{adh}$ of 1.42 J/m$^2$ was within 5% of the 1.48 J/m$^2$ value obtained by converting Nahor *et al.'s* experimentally measured

Ni[$1\bar{1}0$](111)||YSZ[$1\bar{1}0$](111) interface energy and surface energies. The interface energy was measured from Winterbottom analysis of the same Ni[$1\bar{1}0$](111)||YSZ[$1\bar{1}0$](111) interface, equilibrated by annealing at 1350 °C in high-purity inert gas and $H_2$ ($P_{O2} = 10^{-20}$) [65,68]. As $W_{adh}$ is the primary focus of the subsequent sections, LDA functional was considered to give comparable results to the experiments. Further discussion on validation of the model and comparison to previous computational studies of related interfaces can be found in the supplemental materials.

To evaluate *Mechanism II* (the hypothesis that CuO interlayers atop YSZ promote Ag wetting and adhesion), $W_{adh}$ values for Ag(s)/YSZ, Ag/CuO, and CuO/YSZ were calculated using the solid-solid interfaces shown in Fig. 2a-d. Solid interfaces were used because components are eventually solidified and during actual SOFC operations, the strength of braze/YSZ interface was then determined by the adhesion of the two interfaces of Ag(s)/CuO/YSZ. Also, the work of adhesion with liquid Ag is likely to follow the same trend with solid Ag.

As shown in Table 1, the trend of the results from both LDA and GGA-PBE exchange correlations functionals agreed that the presence of CuO leads to a more adherent braze. The closer interface distances shown in Fig. 2 and the $\Delta d$ values of Table 1 also correlated well with the increased $W_{adh}$. The higher $W_{adh}$ resulted in reduction of wetting angle of ~48° when replacing Ag/YSZ with Ag/CuO. Particularly from the prediction by LDA functional, the increment in $W_{adh}$ alone would theoretically be substantial enough to make Ag wettable on CuO (<90°). On the other hand, the high $W_{adh}$ for CuO/YSZ indicates that CuO can firmly adhere to YSZ.

While the liquid-solid interface mimics the braze processing condition and the solid-solid interface represents the solidified braze during SOFC operation, the adhesion and wetting angle between solid-solid and liquid-solid are directly related. Hence the results from one can be

translated to the other. Even though these simulations were performed on solid-solid interfaces, these conclusions should hold for a system with molten Ag for the following reasons: 1) both experimental measurements [58] and thermodynamic derivation [70] have shown that solid Ag surface energies are systematically higher by ~20-33% of those of liquid Ag, the computed $W_{\mathrm{adh}}$ on different interfaces should follow the same trend for liquid and solid Ag. 2) Wetting angles of many liquid metals are known to be a very weak function of temperature (for example, the $W_{\mathrm{adh}}$ of Ag($l$) on $ZrO_2$ only changes by 0.05 J/m$^2$ from 1000 to 1300$^{\circ}$C [8,9,71]). Thus, the absolute values of the $W_{\mathrm{adh}}$ and $\theta_{\mathrm{cal}}$ obtained from the solid-solid interface will be overestimated due to the higher surface energy of a solid compared to its liquid [58], but the calculated trends in both values are expected to hold at brazing temperatures.

It should be noted that the experimental wetting angles of Ag/CuO listed in Table 1 were not taken from pristine experiments as for Ni[$1\bar{1}0$](111)||YSZ[$1\bar{1}0$](111) interface.[65] The contact angle of Ag/CuO [10] was taken from the test of liquid Ag droplet in the air on YSZ with a high concentration of CuO, until the contact angle converged with respect to the amount of CuO. Thus, in practice, the experimental result has a combined effect from *Mechanism I* and *II*. Nevertheless, these experiments show similar contact angle change that can be interpreted from the present study. We have shown that in *Mechanism I,* the presence of oxygen in Ag/YSZ can reduce the contact angle by ~38$^{\circ}$, and forming CuO on YSZ will further reduce the contact angle by ~48$^{\circ}$ from *Mechanism II*, yielding an overall ~86$^{\circ}$ reduction in contact angle when braizing in the air. This is consistent with the experimentally observed 110$^{\circ}$ drop in contact angle (from 120$^{\circ}$ to 10$^{\circ}$). [10]. The rest of the discrepancy can be attributed to the use of solid-solid interface in the simulation and liquid-solid interface in experiments.

### 3.3 Identification of Other Potential Oxide-Forming Alloying Elements

A descriptor that correlates a simple interface structure and bond strength to interface energy at the Ag/oxide interfaces was identified to facilitate the search for potential oxides. The descriptor was based on the results from the projected density of states (PDOS, Fig. S4), which is discussed in the Supplemental Materials and indicates that interfacial bonding occurred primarily from the metal-oxygen bonds. The calculations pertaining to descriptors were performed using LDA functional only as results from previous sections indicate comparable $W_{\mathrm{adh}}$ to experiments.

### 3.3.1 Formulation of a Descriptor Using $\gamma_{12}$ and $W_{\mathrm{adh}}$ in a Predictive Model

The aforementioned descriptor was developed based on the definition of the interface energy, *i.e.* the excess energy introduced by the interface compared to the bulk structure. The first assumption used in this descriptor was that no new Ag-oxide phases formed during brazing. Since the Ag-Ag bond strength is much lower than that of metal-oxide bonds, the descriptor was simplified to only account for 1) the number of unsaturated cation and anion bonds per unit surface area, and 2) the energy changes per unit surface area caused when a portion of the oxygen dangling bonds on a surface was replaced with the newly formed Ag-O bonds across the oxide-Ag interface. This leads to the newly formulated the descriptor ($\chi_{\mathrm{MO}}$):

$$\chi_{\mathrm{MO}} = \frac{f\left((N_{\mathrm{M}} + N_{\mathrm{O}}) \times |E_{\mathrm{M-O}}|\right) - (N_{\mathrm{O}} \times |E_{\mathrm{Ag-O}}|)}{A_{\mathrm{MO}}} \qquad \text{(Eqn. 3)}$$

where $N_{\mathrm{M}}$ and $N_{\mathrm{O}}$ were the number of dangling bonds on the surface cation and oxygen atoms, respectively, in an oxide surface unit cell, $E_{\mathrm{M-O}}$ was the bond enthalpy of the oxide as defined by oxide formation enthalpy ($\Delta H_{\mathrm{f,MO}}$) divided by the number of bonds in a unit cell, $E_{\mathrm{Ag-O}}$ was the bond enthalpy of silver oxide ($Ag_2O$), and $A_{\mathrm{MO}}$ was the surface area of an oxide unit surface. $f$ was an empirical structure factor assigned to be 1 for all studied oxides, except most of the

corundum oxides such as $Al_2O_3$, $Cr_2O_3$ and $In_2O_3$ which, as highlighted in Fig. 4b, contained protruding surface cations necessitating the use of $f$=2 (further explained in the next paragraph).

Figure 4 shows the surface and interface structures used to calculate the descriptors for three sample oxides: CaO , α-$Al_2O_3$, and $Fe_2O_3$. Figure 4a shows that on the {100} surface of CaO, both Ca and O have one dangling bond (resulting in $N_{\mathrm{Ca}} = 1$ and $N_{\mathrm{O}} = 1$). Dividing an LDA-calculated $\Delta H_{\mathrm{f,CaO}}$ = -6.78 eV (which is comparable to -6.39 eV obtained by extrapolating NIST database data down to 0 K), by the 6 Ca-O bonds per unit cell yields $E_{\mathrm{Ca-O}} = \frac{-6.78}{6}$ = -1.13 eV/bond. In a similar fashion, LDA calculated the relaxed structure $E_{\mathrm{Ag-O}}$ to be -0.14 eV/bond. The relaxed CaO {100} surface has $A_{\mathrm{CaO}}$ of 11.14 Å$^2$. Together with $f$=1, this yielded a $\chi_{\mathrm{CaO}}$ of 0.19 eV/Å$^3$. Figure 4b shows the surface structure of corundum-type oxides, represented by $Al_2O_3$ (0001) and its relaxed interface with Ag. It has a $N_{\mathrm{Al}} = 3$, a $N_{\mathrm{O}} = 3$, a LDA calculated relaxed structure $A_{\mathrm{Al_2O_3}} = 19.40$ Å$^2$, and a LDA calculated relaxed structure $\Delta H_{\mathrm{f,AlO_3}}$ = -17.42 eV which resulted in a $E_{\mathrm{Al-O}} = -\frac{17.42}{12}$ = -1.45 eV, with an $f$ factor of 2, this yielded a $\chi_{\mathrm{Al_2O_3}}$ of 0.85 eV/Å$^3$. Among all the corundum oxides tested, namely $Al_2O_3$, $Cr_2O_3$, $In_2O_3$, and $Rh_2O_3$ all have protruding (0001) surface cation (pointed out by the yellow arrow in Fig. 4). The protruded cation prevents the silver slab to get closer to the oxygen layer (Fig. 4b), where the $\Delta d$ of Ag/$Al_2O_3$ is 2.58 Å compared to 1.81 Å in Ag/$Fe_2O_3$ (Fig 4c). This behavior may account for the weak Ag/$Al_2O_3$ bonding reported in the literature.[72] Consequently, to account for the increase in interfacial energy, $f$=2 is used for most of the corundum oxides with protruded cations. It is interesting to note that all the corundum type oxides studied here, except $Fe_2O_3$, had protruding (0001) surface cations that necessitated the use of $f$ = 2. In $Fe_2O_3$, whose cation, $Fe^{3+}$, submerges beneath the oxygen layer after the relaxation so it does not interfere the Ag-O bonds (Fig. 4c). This means that there

is no need to increase the structure factor, so the calculation of $\chi_{MO}$ for $Fe_2O_3$ follows the similar manner as $Al_2O_3$ but with $f$=1 for the smooth top O layer. Table S1 of the Supplemental Materials summarizes all the descriptor calculations performed in the present work.

The unique behavior of $Fe_2O_3$ may be due to its strong *3d* electron interaction with the oxygen polyhedron. In $M_2O_3$ corundum oxides bulk structure, the cation $M^{3+}$ occupies 2/3 of the oxygen octahedral sites. On the $M^{3+}$ terminated surface, the protruding $M^{3+}$ without unpaired electrons will relax toward the oxygen due to electrostatic interactions, as for $Al_2O_3$ and $In_2O_3$. Comparing $Fe^{3+}(3d^5)$, $Rh^{3+}(4d^6)$, and $Cr^{3+}(3d^3)$ in $Cr_2O_3$, $Rh_2O_3$, and $Fe_2O_3$, respectively, the interaction between the oxygen octahedral may attract $Fe^{3+}(3d^5)$, which has the most unpaired *d*-electrons to move underneath the top oxygen layer. Due to the complexity of computing strong correlated d-electrons in transition metal oxides, more research is warranted.

It should be noted that the use of surface energetics, classical view of charge transfer, and metal-oxide formation energies, to formulate a descriptor to relate directly to interface energy $\gamma_{12}$ and work of adhesion $W_{adh}$ for Ag/oxide interface has been tried, but we did not find no strong correlation.

### 3.3.2 Descriptor-Based Prediction of Interface Energy and $W_{adh}$

Figure 5a shows the DFT computed interface energy and its relationship with $\sigma_{MO}$ in various types of oxides. The interface energy monotonically increases with the descriptor. The simple descriptor defined in Eqn. 3 enables assessment of oxide properties that will lead to high or low interface energy. Two factors can affect the interface energy; one is the oxide bond energy ($|E_{M-O}|$), which has a chemical nature. The other is the density of the dangling bonds, which depends on the geometry of the surface. The increase in either of these would increase the value

of descriptor, and hence the interface energy. In Fig. 5a, the interplay between these two factors is evident. For example, $ZrO_2$, which has the highest bond energy among oxides in this study (-2.39 eV/bond), did not show the highest interface energy. $Al_2O_3$ has the highest interface energy, although its bond energy of -1.45 eV/bond is not as large as $ZrO_2$. This is due to a different surface geometry, as $Al_2O_3$ contains 1.7 times larger surface dangling bond density than $ZrO_2$. In fact, the oxides with higher interface energy with Ag (Fig 5a) was dominated by corundum type oxides. On the other hand, in the lower region of interface energy, although $Rb_2O$ and CdO both had similarly low bond energy of -0.46 and -0.43 eV/bond, respectively, $Cu_2O$ with the bond energy of -0.51 eV/bond exhibited much lower interface energy due to its low dangling bond density of 0.07 bonds/Å$^2$, compared to 0.11 and 0.18 bonds/Å$^2$ of $Rb_2O$ and CdO. This simple descriptor also means that if oxides of interest possessed the same surface geometry, and likely the same crystal structures, the descriptor could be approximated by just the chemical feature – the bond formation energy, or equivalently oxide formation energy. This trend can be seen in Fig 5, as different crystalline structures were labeled with different symbols. Therefore, for oxides within the same crystalline family, both interface energy and $W_{\mathrm{adh}}$ can be simplified to correlate with their formation energies as shown in Fig. S6 for corundum and rock salt oxides and suggested by Li *et al*. [40].

The results plotted in Fig 5a demonstrated that the descriptor is well-correlated with the DFT calculated interface energy, which increases with the descriptor. A fitting equation:

$$\gamma_{12}^{\mathrm{pred}} = 0.55 \ln(\chi_{\mathrm{MO}}) + 2.43 \qquad \text{(Eqn. 4)}$$

was obtained with a coefficient of determination $R^2 = 0.95$. Hence, this equation can be used to estimate interface energy ($\gamma_{12}^{\mathrm{pred}}$) solely based on the descriptor. The predicted interface energy

was then used to predict $W_{\mathrm{adh}}^{\mathrm{pred}}$ as defined by Eqn. 1, with tabulated surface energies, which is easier compute with DFT calculations. In this study, the surfaces of these oxides were selected based upon a criterion of being the lowest surface energy. The individual surface energy of these oxides is tabulated in Table S1 and discussed in the Supplemental Materials.

The predicted $W_{\mathrm{adh}}^{\mathrm{pred}}$ was plotted against the DFT-calculated $W_{\mathrm{adh}}$ in Fig 5b, which also demonstrates satisfactory accuracy (Fig. 5b). The conclusion obtained from the two ends of the $W_{\mathrm{adh}}$ plot indicated that $ZrO_2$ as well as YSZ were among the most difficult oxides for Ag to be wetted. On the other hand, while both $Fe_2O_3$ and $Rh_2O_3$ provided high adhesion, like CuO, both of them are not stable under SOFC reducing environment ($Fe_2O_3$ would be reduced at temperature above 587 °C). Within Fig. 5b, a candidate with the highest $W_{\mathrm{adh}}$ that would be stable in a reducing environment is $In_2O_3$, but its $W_{\mathrm{adh}}$ is only 1.03 J/m$^2$, 0.4 J/m$^2$ lower than CuO.

The descriptor was also employed to screen more single cation oxides but, among those, none gave a higher $W_{\mathrm{adh}}$ with Ag than CuO. For example, a rutile $SnO_2$ (110) was predicted based on the descriptor to have $W_{\mathrm{adh}}$ of 1.23 J/m$^2$. For validation purposes, the DFT-calculation gave $W_{\mathrm{adh}}$ =1.10 J/m$^2$, using a half-sandwich interface model. The $W_{\mathrm{adh}}$ translated to a borderline wetting contact angle of 90°, which when combined with the effect from dissolved oxygen in Ag(*l*) could enable Ag wetting, although it would not be as good as CuO. In addition, $SnO_2$ is a bit more resistant to the reduction environment, as it is expected to be stable up to 647 °C according to Ellingham Diagram. It have been suggested that $V_2O_5$ could be another potential oxides;[23] however, due to the step-like structure of the (010) surface, a smooth surface of Ag used in the present descriptor model could not accurately determine $W_{\mathrm{adh}}$ of this interface. In conclusion, our

screening of monocation oxides could not identify a candidate that would yield similar or higher $W_{\mathrm{adh}}$ than CuO, while not being cost-prohibitive or reduced in SOFC operating conditions.

### 3.3.3 Identification of Complex Oxides and Ternary Braze Alloy Design

Since the simple oxide search did not predict many candidates that could potentially be 1) better than CuO in enhancing $W_{\mathrm{adh}}$ and 2) stable in a reducing SOFC environment, the descriptor was used to search for potential multi-cation oxides. First, the descriptor was used to explore multi-cation oxides with lower descriptor values that lead to lower interface energy (since a low interface energy is a necessary but not sufficient condition for a high work of adhesion). Then, the surface energies were computed by DFT. The stable surface for all delafossite oxides was chosen to be O-terminated (0001) surfaces, based on experimental and computational evidence [73–75]. Predicting the interface energy $\gamma_{12}^{\mathrm{pred}}$ from the descriptor using Eqn. 4, and the DFT computed surface energies, the $W_{\mathrm{adh}}$ was first predicted before the DFT interface model was constructed. From this, it was found that several oxides with a delafossite structure could exhibit strong adhesion due to their high surface energy relative to a low predicted interface energy (Table 3). For comparison, CuO is listed as well. While some delafossite oxides exhibited low adhesion ~0.7 J/m$^2$ with Ag, such as $CuCrO_2$ and $CuFeO_2$, several delafossite oxides, $CuAlO_2$, $CuGaO_2$, and $CuInO_2$, showed higher predicted $W_{\mathrm{adh}}$ (2.3~2.6 J/m$^2$) with Ag than CuO (1.43 J/m$^2$).

$Cu_3TiO_4$(010) also yielded a predicted $W_{\mathrm{adh}}$ of 2.12 J/m$^2$, which is higher than that of CuO. $Cu_3TiO_4$ has a similar structure to delafossite, and its (010) surface is equivalent to the (0001) surface of delafossite oxides. The increase of $W_{\mathrm{adh}}$ on $Cu_3TiO_4$ surface could also explain the observed enhanced braze wettability when $TiO_2$ is added to the Ag–CuO system [14]. $TiO_2$ itself is not the likely cause of wettability enhancement, as predictions for both the rutile $TiO_2$(110) and

anatase $TiO_2$(101) structures yielded $W_{adh}$ of only 0.40 and 0.56 J/m$^2$, respectively. However, $TiO_2$ could react with CuO or $Cu_2O$ to form $Cu_3TiO_4$ [76,77]. Therefore, the addition of Cu and Ti to Ag, with modification of brazing gas environment and temperature conditions to purposely generate $Cu_3TiO_4$ on the YSZ surface could also further enhance the wetting of Ag. Also, as indicated by its formation energy (-13.12 eV) on the Ellingham diagram, $Cu_3TiO_4$ will be stable in a reducing SOFC environment.

Another interesting oxide is $CuAlO_2$. The formation of $CuAlO_2$ would be favorable in certain conditions as the $CuAlO_2$ formation energy was calculated to be -9.70 eV, which is comparable to -9.74 eV for ½($Al_2O_3$ + $Cu_2O$). Experimental phase diagrams indicate that $CuAlO_2$ is stable at high temperature, especially in the brazing and SOFC operating temperature range [78]. Putting the calculated formation energy of $CuAlO_2$ on the Ellingham diagram shows that it is stable in a reducing environment. To further investigate this promising oxide and also obtain the accurate $W_{adh}$, DFT calculations were performed (Fig. 6a). The DFT-calcualted $W_{adh}$ of Ag/$CuAlO_2$. is 3.04 J/m$^2$, almost twice of that at the Ag/CuO interface. The changes in PDOS through formation of this interface shown in Fig. 6b correspond well to its high $W_{adh}$, where oxygen *p*-states moved from high-energy antibonding (-2 to 0 eV) to bonding states at energies below the metal *d*-states (~ -8 eV). This high adhesion will lead to complete wetting (0$^\circ$). Moreover, DFT calculation using half-sandwich model also indicate strong adhesion ($W_{adh}$= 2.04 J/m$^2$) between $CuAlO_2$ and YSZ. Overall, this is in accordance with reports that the greater extent of $CuAlO_2$ formed from the unintended reaction of CuO with $Al_2O_3$, the lower contact angle of Ag [25].

The other delafossites, $CuGaO_2$ and $CuInO_2$, and $Cu_3TiO_4$ were predicted to yield similarly high $W_{adh}$ are therefore are expected to yield similar results. However, the formation energy of $CuInO_2$, which is the highest among investigated delafossites (-5.70 eV), was only -0.52 eV below

the hydrogen line in Ellingham diagram. Given that LDA tends to overestimate bonding energy, it is more prudent to assume that $CuInO_2$ would not be stable in a reducing SOFC environment.

Therefore, several oxide interlayers, $CuAl(or\ Ga)O_2$ or $Cu_3TiO_4$, that could improve the interfacial strength were identified via our computational search. In order to form these oxide layers, the complex oxide could either be pre-sputtered or coated on the YSZ surface before brazing or be directly added to Ag, as similar methods have been used for Ag-CuO system [25,79]. Alternatively, alloying Ag with a mixture of Cu and Al (or Ga, Ti) and fine tuning the brazing gas environment and temperature conditions to intentionally maximize the formation of $CuAl(or\ Ga)O_2$ or $Cu_3TiO_4$ could also improve the interfacial strength. It should be noted that, according to the original definition, in order to be classified as a RAB component, the oxides formed by the secondary metals in air must be at least be partially soluble in Ag [80] in order to avoid forming thick oxide scale on the liquid surface to inhibit wetting. The oxide solubility, the impact of these alloy or oxide additions on the melting temperature, can be considered in follow-up studies. Nevertheless, these examples suggest that ternary alloy systems may offer many more possibilities. The discovery of potential oxides can be expanded beyond the examples given here.

## 5. CONCLUSION

The RAB process is a promising solution to solve wetting and adhesion problem of Ag on an YSZ surface for sealing applications as well as providing practicality for industrial settings. As the current Ag-CuO system has a short-coming due to pore formation from reduction of CuO to Cu, there are alternative approaches of other oxide interlayer design that may be effective. Using DFT calculations and interface models, the present paper has identified the two primary mechanisms that enabled Ag to wet on YSZ surfaces, including 1) formation of Ag–O clusters at the Ag/YSZ interface from the oxygen in solution (*Mechanism I*), and 2) enhanced $W_{adh}$ by

formation of a CuO scale on top of the YSZ (*Mechanism II*). *Mechanism I* reduces the wetting angle by 20~25˚, which is a smaller effect than the second mechanism, as the CuO scale can reduce the wetting angle by ~45˚, changing the metal from non-wetting to wetting. The electronic analysis of the involved interfaces shows that interactions between Ag and oxygen atoms of the oxide dominates the interfacial bonding. With this knowledge, a simple descriptor for calculation of interface energy was developed to reduce the dependence on expensive interface calculations. With known surface energy, which is much more easily calculated, the descriptor can also be used for prediction of $W_{\mathrm{adh}}$. Several single cation metal oxides were considered, but the number of those with $W_{\mathrm{adh}}$ comparable to CuO and tolerant of a reducing environment were few. For example, none of the investigated metal oxides, with crystalline structures of rock salt, fluorite, and anti-fluorite, showed high $W_{\mathrm{adh}}$. However, by expanding the search to multi-cation oxides, several promising candidates in oxides with delafossite structure, such as $CuAlO_2$, $CuGaO_2$, and $Cu_3TiO_4$, were discovered to double the work of adhesion of CuO with Ag. The study provides insight to geometry and bonding energy of metal-oxide interfaces with implications beyond just Ag and YSZ interfaces. The convenient search also opens new pathways to develop potential ternary Ag-oxide braze alloys with enhanced adhesion and wetting on YSZ.

**Acknowledgment**

This work was supported by the Department of Energy under Award Number DE-FE0023315.

**REFERENCES**

[1] E. Saiz, R.M. Cannon, A.P. Tomsia, High-temperature wetting and the work of adhesion in metal/oxide systems, Annu. Rev. Mater. Res. 38 (2008) 197–226.
[2] J.W. Fergus, Sealants for solid oxide fuel cells, J. Power Sources. 147 (2005) 46–57.
[3] Braze alloy containing particulate material, 2005. https://patents.google.com/patent/EP1616657A1/en (accessed November 8, 2017).
[4] Method and apparatus for gasketing a fuel cell, 2004. https://patents.google.com/patent/EP1492190A2/en (accessed November 8, 2017).

[5] S. Le, Z. Shen, X. Zhu, X. Zhou, Y. Yan, K. Sun, N. Zhang, Y. Yuan, Y. Mao, Effective Ag–CuO sealant for planar solid oxide fuel cells, J. Alloys Compd. 496 (2010) 96–99.
[6] Q. Zhou, T.R. Bieler, J.D. Nicholas, Transient porous nickel interlayers improved silver-based solid oxide fuel cell brazes, submitted to Acta Mater.
[7] P. Nikolopoulos, G. Ondracek, D. Sotiropoulou, Wettability and interfacial energies between zirconia ceramic and liquid metals, Ceram. Int. 15 (1989) 201–206.
[8] P. Nikolopoulos, D. Sotiropoulou, Wettability between zirconia ceramics and the liquid metals copper, nickel and cobalt, J. Mater. Sci. Lett. 6 (1987) 1429–1430.
[9] M. Ueki, M. Naka, I. Okamoto, Wettability of some metals against zirconia ceramics, J. Mater. Sci. Lett. 5 (1986) 1261–1262.
[10] K.S. Weil, J.Y. Kim, J.S. Hardy, Reactive air brazing: A novel method of sealing sofcs and other solid-state electrochemical devices, Electrochem. Solid-State Lett. 8 (2005) A133–A136.
[11] B. Kuhn, T. Beck, Achievements in reactive air brazing, Adv. Eng. Mater. 16 (2014) 1413–1414.
[12] A.M. Meier, P. Chidambaram, G.R. Edwards, A comparison of the wettability of copper-copper oxide and silver-copper oxide on polycrystalline alumina, J. Mater. Sci. 30 (1995) 4781–4786.
[13] J.Y. Kim, J.S. Hardy, K.S. Weil, Effects of CuO content on the wetting behavior and mechanical properties of a Ag–CuO braze for ceramic joining, J. Am. Ceram. Soc. 88 (2005) 2521–2527.
[14] J.Y. Kim, J.S. Hardy, K.S. Weil, Silver-copper oxide based reactive air braze for joining yttria-stabilized zirconia, J. Mater. Res. 20 (2005) 636–643.
[15] H. Chen, L. Li, R. Kemps, B. Michielsen, M. Jacobs, F. Snijkers, V. Middelkoop, Reactive air brazing for sealing mixed ionic electronic conducting hollow fibre membranes, Acta Mater. 88 (2015) 74–82.
[16] S. Hashimoto, Y. Fukuda, M. Kuhn, K. Sato, K. Yashiro, J. Mizusaki, Oxygen nonstoichiometry and thermo-chemical stability of $La_{0.6}Sr_{0.4}Co_{1-y}Fe_yO_{3-\delta}$ (y=0.2, 0.4, 0.6, 0.8), Solid State Ion. 181 (2010) 1713–1719.
[17] Chen, Yu, S.B. Adler, Thermal and chemical expansion of Sr-doped lanthanum cobalt oxide ($La_{1-x}Sr_xCoO_{3-\delta}$), Chem. Mater. 17 (2005) 4537–4546.
[18] S.R. Bishop, K.L. Duncan, E.D. Wachsman, Thermo-chemical expansion in strontium-doped lanthanum cobalt iron oxide, J. Am. Ceram. Soc. 93 (2010) 4115–4121.
[19] E.M. Pfaff, A. Kaletsch, C. Broeckmann, Design of a mixed ionic/electronic conducting oxygen transport membrane pilot module, Chem. Eng. Technol. 35 (2012) 455–463.
[20] J. Cao, X. Si, W. Li, X. Song, J. Feng, Reactive air brazing of YSZ-electrolyte and Al2O3-substrate for gas sensor sealing: Interfacial microstructure and mechanical properties, Int. J. Hydrog. Energy. 42 (2017) 10683–10694.
[21] K.S. Weil, J.S. Hardy, J.Y. Kim, Oxidation ceramic to metal braze seals for applications in high temperature electrochemical devices and method of making, US7055733 B2, 2006. http://www.google.com/patents/US7055733.

[22] V. Middelkoop, Reactive air brazing (RAB) for gas separation membranes, in: E. Drioli, L. Giorno (Eds.), Encycl. Membr., Springer Berlin Heidelberg, Berlin, Heidelberg, 2016: pp. 1710–1713.
[23] J.S. Hardy, J.Y. Kim, K.S. Weil, Joining mixed conducting oxides using an air-fired electrically conductive braze, J. Electrochem. Soc. 151 (2004) J43–J49.
[24] Q. Zhou, T.R. Bieler, J.D. Nicholas, Reactive-element-free, silver-based brazes for SOFC applications, ECS Trans. 78 (2017) 1759–1767.
[25] R. Chatzimichail, G. Triantafyllou, F. Tietz, P. Nikolopoulos, Interfacial properties of (Ag + CuO) brazes used as sealing materials in SOFC stacks, J. Mater. Sci. 49 (2014) 300–313.
[26] I. Barin, Compilation of Thermochemical Data, in: Thermochem. Data Pure Subst., Wiley-VCH Verlag GmbH, 1995: pp. 33–34.
[27] J. Hu, D. Li, J.G. Lu, R. Wu, Effects on electronic properties of molecule adsorption on CuO surfaces and nanowires, J. Phys. Chem. C. 114 (2010) 17120–17126.
[28] Y. Maimaiti, M. Nolan, S.D. Elliott, Reduction mechanisms of the CuO(111) surface through surface oxygen vacancy formation and hydrogen adsorption, Phys. Chem. Chem. Phys. 16 (2014) 3036–3046.
[29] A. Eichler, G. Kresse, First-principles calculations for the surface termination of pure and yttria-doped zirconia surfaces, Phys. Rev. B. 69 (2004) 045402.
[30] S. Takemoto, T. Tada, Zirconium-peroxo embedded in non-stoichiometric yttria stabilized zirconia (110) from first-principles, Solid State Ion. 285 (2016) 215–221.
[31] T. Sasaki, K. Matsunaga, H. Ohta, H. Hosono, T. Yamamoto, Y. Ikuhara, Atomic and Electronic Structures of Ni/YSZ(111) Interface, Mater. Trans. 45 (2004) 2137–2143.
[32] M. Shishkin, T. Ziegler, The oxidation of $H_2$ and $CH_4$ on an oxygen-enriched yttria-stabilized zirconia surface: A theoretical study based on density functional theory, J. Phys. Chem. C. 112 (2008) 19662–19669.
[33] H. Ding, A.V. Virkar, F. Liu, Defect configuration and phase stability of cubic versus tetragonal yttria-stabilized zirconia, Solid State Ion. 215 (2012) 16–23.
[34] S.C. Ammal, A. Heyden, Combined DFT and microkinetic modeling study of hydrogen oxidation at the Ni/YSZ anode of solid oxide fuel cells, J. Phys. Chem. Lett. 3 (2012) 2767–2772.
[35] C. Pascual, P. Durán, Subsolidus phase equilibria and ordering in the system $ZrO_2$-$Y_2O_3$, J. Am. Ceram. Soc. 66 (1983) 23–27.
[36] J.I. Beltrán, S. Gallego, J. Cerdá, J.S. Moya, M.C. Muñoz, Internal ceramic Reconstruction weakens metal−$ZrO_2$ adhesion, J. Phys. Chem. B. 108 (2004) 15439–15442.
[37] S.E. Kul'kova, A.V. Bakulin, S. Hocker, S. Schmauder, Theoretical study of adhesion at the metal-zirconium dioxide interfaces, Tech. Phys. 58 (2013) 325–334.
[38] J.I. Beltrán, M.C. Muñoz, *Ab initio* study of decohesion properties in oxide/metal systems, Phys. Rev. B. 78 (2008) 245417.
[39] O.I. Malyi, V.V. Kulish, K. Bai, P. Wu, Z. Chen, A computational study of the effect of alloying additions on the stability of Ni/c-$ZrO_2$ interfaces, Surf. Sci. 611 (2013) 5–9.

[40] J.G. Li, Wetting and interfacial bonding of metals with ionocovalent oxides, J. Am. Ceram. Soc. 75 (1992) 3118–3126.
[41] K. Scott Weil, C.A. Coyle, J.T. Darsell, G.G. Xia, J.S. Hardy, Effects of thermal cycling and thermal aging on the hermeticity and strength of silver–copper oxide air-brazed seals, J. Power Sources. 152 (2005) 97–104.
[42] E. Skiera, J. Brandenberg, C. Li, T. Beck, L. Singheiser, B. Kuhn, Mechanical properties of reactive air brazed (RAB) metal/ceramic joints. Part 1: Visco-plastic deformation of silver-based reactive air brazes, Adv. Eng. Mater. 16 (2014) 1462–1467.
[43] J.Y. Kim, J.S. Hardy, S. Weil, Dual-atmosphere tolerance of Ag–CuO-based air braze, Int. J. Hydrog. Energy. 32 (2007) 3655–3663.
[44] A. Pönicke, J. Schilm, M. Kusnezoff, A. Michaelis, Aging behavior of reactive air brazed seals for SOFC, Fuel Cells. 15 (2015) 735–741.
[45] J.P. Perdew, K. Burke, M. Ernzerhof, Generalized gradient approximation made simple, Phys. Rev. Lett. 77 (1996) 3865–3868.
[46] A.D. Becke, Density-functional exchange-energy approximation with correct asymptotic behavior, Phys. Rev. A. 38 (1988) 3098–3100.
[47] G. Kresse, D. Joubert, From ultrasoft pseudopotentials to the projector augmented-wave method, Phys. Rev. B. 59 (1999) 1758–1775.
[48] S.L. Dudarev, G.A. Botton, S.Y. Savrasov, C.J. Humphreys, A.P. Sutton, Electron-energy-loss spectra and the structural stability of nickel oxide: An LSDA+U study, Phys. Rev. B. 57 (1998) 1505–1509.
[49] N.J. Mosey, P. Liao, E.A. Carter, Rotationally invariant ab initio evaluation of Coulomb and exchange parameters for DFT+U calculations, J. Chem. Phys. 129 (2008) 014103.
[50] N. Mansourian-Hadavi, S. Wansom, N.H. Perry, A.R. Nagaraja, T.O. Mason, L. Ye, A.J. Freeman, Transport and band structure studies of crystalline $ZnRh_2O_4$ Phys. Rev. B. 81 (2010) 075112.
[51] O. Bengone, M. Alouani, P. Blöchl, J. Hugel, Implementation of the projector augmented-wave LDA+U method: Application to the electronic structure of NiO, Phys. Rev. B. 62 (2000) 16392–16401.
[52] D.A. Andersson, S.I. Simak, B. Johansson, I.A. Abrikosov, N.V. Skorodumova, Modeling of $CeO_2$, $Ce_2O_3$, and $CeO_{2-x}$ in the LDA+U formalism, Phys. Rev. B. 75 (2007) 035109.
[53] Y. Peng, Z. Zhang, T. Viet Pham, Y. Zhao, P. Wu, J. Wang, Density functional theory analysis of dopants in cupric oxide, J. Appl. Phys. 111 (2012) 103708.
[54] Z. Zhao, X. He, J. Yi, C. Ma, Y. Cao, J. Qiu, First-principles study on the doping effects of nitrogen on the electronic structure and optical properties of $Cu_2O$, RSC Adv. 3 (2012) 84–90.
[55] J. Chevalier, L. Gremillard, A.V. Virkar, D.R. Clarke, The tetragonal-monoclinic transformation in zirconia: lessons learned and future trends, J. Am. Ceram. Soc. 92 (2009) 1901–1920.
[56] M.A. Idris, T. Bak, S. Li, J. Nowotny, Effect of segregation on surface and near-surface chemistry of yttria-stabilized zirconia, J. Phys. Chem. C. 116 (2012) 10950–10958.

[57] A.J.A. Winnubst, P.J.M. Kroot, A.J. Burggraaf, AES/STEM grain boundary analysis of stabilized zirconia ceramics, J. Phys. Chem. Solids. 44 (1983) 955–960.
[58] V.K. Kumikov, K.B. Khokonov, On the measurement of surface free energy and surface tension of solid metals, J. Appl. Phys. 54 (1983) 1346–1350.
[59] F.G. Donnan, T.W.A. Shaw, The solubility of oxygen in molten silver, J. Soc. Chem. Ind. 29 (1910) 987–989.
[60] A.D. Kirshenbaum, J.A. Cahill, A.V. Grosse, The density of liquid silver from its melting point to its normal boiling point 2450°K, J. Inorg. Nucl. Chem. 24 (1962) 333–336.
[61] Module, Forcite. "Material Studio 6.0.," Accelrys Inc., San Diego, CA, 2011.
[62] H. Sun, Z. Jin, C. Yang, R.L.C. Akkermans, S.H. Robertson, N.A. Spenley, S. Miller, S.M. Todd, COMPASS II: Extended coverage for polymer and drug-like molecule databases, J. Mol. Model. 22 (2016) 47.
[63] W.X. Zhang, C. He, Melting of Cu nanowires: A study using molecular dynamics simulation, J. Phys. Chem. C. 114 (2010) 8717–8720.
[64] C.N.J. Wagner, H. Ocken, M.L. Joshi, Interference and radial distribution functions of liquid copper, silver, tin, and mercury, Z. Für Naturforschung A. 20 (2014) 325–335.
[65] H. Nahor, H. Meltzman, W.D. Kaplan, Ni–YSZ(111) solid–solid interfacial energy, J. Mater. Sci. 49 (2014) 3943–3950.
[66] H. Meltzman, D. Chatain, D. Avizemer, T.M. Besmann, W.D. Kaplan, The equilibrium crystal shape of nickel, Acta Mater. 59 (2011) 3473–3483.
[67] A. Tsoga, P. Nikolopoulos, Surface and grain-boundary energies in yttria-stabilized zirconia (YSZ-8 mol%), J. Mater. Sci. 31 (1996) 5409–5413.
[68] W.L. Winterbottom, Equilibrium shape of a small particle in contact with a foreign substrate, Acta Metall. 15 (1967) 303–310.
[69] J.T. Darsell, K.S. Weil, Experimental determination of phase equilibria in the silver–copper oxide system at high temperature, Scr. Mater. 56 (2007) 1111–1114.
[70] W.R. Tyson, W.A. Miller, Surface free energies of solid metals: Estimation from liquid surface tension measurements, Surf. Sci. 62 (1977) 267–276.
[71] D. Sotiropoulou, P. Nikolopoulos, Work of adhesion in $ZrO_2$-liquid metal systems, J. Mater. Sci. 28 (1993) 356–360.
[72] W. Zhang, J.R. Smith, Stoichiometry and adhesion of Nb/$Al_2O_3$, Phys. Rev. B. 61 (2000) 16883–16889.
[73] N. Tsuboi, T. Moriya, S. Kobayashi, H. Shimizu, K. Kato, F. Kaneko, Characterization of $CuAlO_2$ thin films prepared on sapphire substrates by reactive sputtering and annealing, Jpn. J. Appl. Phys. 47 (2008) 592.
[74] C.H. Shih, B.H. Tseng, Formation mechanism of $CuAlO_2$ prepared by rapid thermal annealing of $Al_2O_3$/$Cu_2O$/sapphire sandwich structure, Phys. Procedia. 32 (2012) 395–400.
[75] Q.J. Liu, Z.T. Liu, Theoretical insights into structural–electronic relationships and relative stability of the Cu-, Al- and O-terminated $CuAlO_2$(0001) surfaces, Vacuum. 107 (2014) 90–98.
[76] D. Hennings, Phase equilibria and thermodynamics of the double oxide phase $Cu_3TiO_4$, J. Solid State Chem. 31 (1980) 275–279.

[77] S. Derling, T. Müller, H.-P. Abicht, K.-H. Felgner, H.T. Langhammer, Copper oxide as a sintering agent for barium titanate based ceramics, J. Mater. Sci. 36 (2001) 1425–1431.
[78] K.T. Jacob, C.B. Alcock, Thermodynamics of $CuAlO_2$ and $CuAl_2O_4$ and phase equilibria in the system $Cu_2O$-CuO-$Al_2O_3$, J. Am. Ceram. Soc. 58 (1975) 192–195.
[79] K.M. Erskine, A.M. Meier, S.M. Pilgrim, Brazing perovskite ceramics with silver/copper oxide braze alloys, J. Mater. Sci. 37 (2002) 1705–1709.
[80] K.S. Weil, J.S. Hardy, J.P. Rice, J.Y. Kim, Brazing as a means of sealing ceramic membranes for use in advanced coal gasification processes, Fuel. 85 (2006) 156–162.

**Table 1**. The average interface distance ($\Delta d$), work of adhesion ($W_{adh}$), calculated wetting angles ($\theta_{cal}$), and experimental ($\theta_{exp}$) for Ni/YSZ interface and systems involved in Ag–CuO/YSZ braze.

| Interface Systems | XC | $\Delta d$ (Å) | $W_{adh}$ (J/m$^2$) | $\theta_{cal}$ | $\theta_{exp}$ |
|---|---|---|---|---|---|
| Ni[1$\bar{1}$0](111)\|\|YSZ[1$\bar{1}$0](111) | GGA | 2.03 | 0.49 | 138° | 120° [7] |
| | LDA | 2.01 | 1.42 | 118° | |
| Ag(*l*)/YSZ(1 1 1)‡ | GGA | 2.41±0.02 | 0.11±0.01 | 149° | 120° [7] |
| {Ag(*l*)+2O}/YSZ(1 1 1)† | GGA | 2.17±0.04 | 0.43±0.01 | 111° | 90° [69]ǂ |
| Ag[$\bar{3}$ 2 1](1 1 1)\|\|YSZ[$\bar{1}$ 1 0](1 1 1) | GGA | 2.68 | 0.10 | 150° | 120° [7] |
| | LDA | 2.43 | 0.53 | 121° | |
| Ag[1 $\bar{1}$ 0](1 1 1)\|\|CuO[$\bar{1}$ 1 0](1 1 1) | GGA | 2.26 | 0.48 | 112° | 10° [10]ǂ |
| | LDA | 2.11 | 1.43 | 73° | |
| CuO[1 $\bar{3}$ 2](1 1 1)\|\|YSZ[0 $\bar{1}$ 1](1 1 1) | GGA | 1.76 | 0.65 | 96° | – |
| | LDA | 1.71 | 1.11 | 92° | |

‡An interface without dissolved oxygen atoms.
†An interface with dissolved oxygen atoms located initially at the interface.
ǂ Ref [69] and [10] reported sessile drop tests performed in air. The contact angle of Ag/CuO was taken from the test of liquid Ag on YSZ at high concentration of CuO, until the contact angle converged with respect to the amount of CuO on YSZ. [10]

**Table 2**. The surface and interface energetics involved in Ni[$1\bar{1}0$](111)||YSZ[$1\bar{1}0$](111) interface.

| | | $\gamma_{Ni(111)}$ | $\gamma_{YSZ(111)}$ | $\gamma_{Ni-YSZ}$ | $W_{adh}$ |
|---|---|---|---|---|---|
| **DFT computed** | **GGA-PBE** | 1.94 | 0.70 | 2.26 | 0.49 |
| | **LDA** | 2.68 | 1.42‡ | 2.68 | 1.42‡ |
| **Experiment** [65] | | 2.05 [66] | 1.23 [67] | 1.8±0.1 | 1.48 |

‡Because the obtained $W_{adh}$ is coincidentally close to the surface energy of YSZ (based on LDA calculations), the derived interface energy of Ni/YSZ is the same as the Ni surface energy, following Equ. 1.

**Table 3**. The surface energy ($\gamma$), predictor value ($\chi_{\mathrm{MO}}$), and predicted interface energy ($\gamma_{12}^{\mathrm{pred}}$), predicted work of adhesion ($W_{\mathrm{adh}}^{\mathrm{pred}}$), and DFT-calculated work of adhesion ($W_{\mathrm{adh}}$) of the delafossite oxides and $Cu_3TiO_4$.

| **Oxide** | $\boldsymbol{\gamma}$ **(J/m²)** | $\chi_{\mathbf{MO}}$ | $\boldsymbol{\gamma_{12}^{\mathrm{pred}}}$ **(J/m²)** | $W_{\mathrm{adh}}^{\mathrm{pred}}$ **(J/m²)** | $W_{\mathrm{adh}}$ **(J/m²)** |
|---|---|---|---|---|---|
| CuO | 1.16 | 0.066 | 0.92 | 1.34 | 1.43 |
| $CuAlO_2(0001)$ | 3.02 | 0.156 | 1.41 | 2.71 | 3.04 |
| $CuCrO_2(0001)$ | 1.40 | 0.150 | 1.39 | 1.11 | - |
| $CuFeO_2(0001)$ | 1.08 | 0.141 | 1.36 | 0.82 | - |
| $CuGaO_2(0001)$ | 2.82 | 0.094 | 1.13 | 2.79 | - |
| $CuInO_2(0001)$ | 2.54 | 0.061 | 0.89 | 2.75 | - |
| $Cu_3TiO_4(010)$ | 1.76 | 0.086 | 1.08 | 1.78 | - |

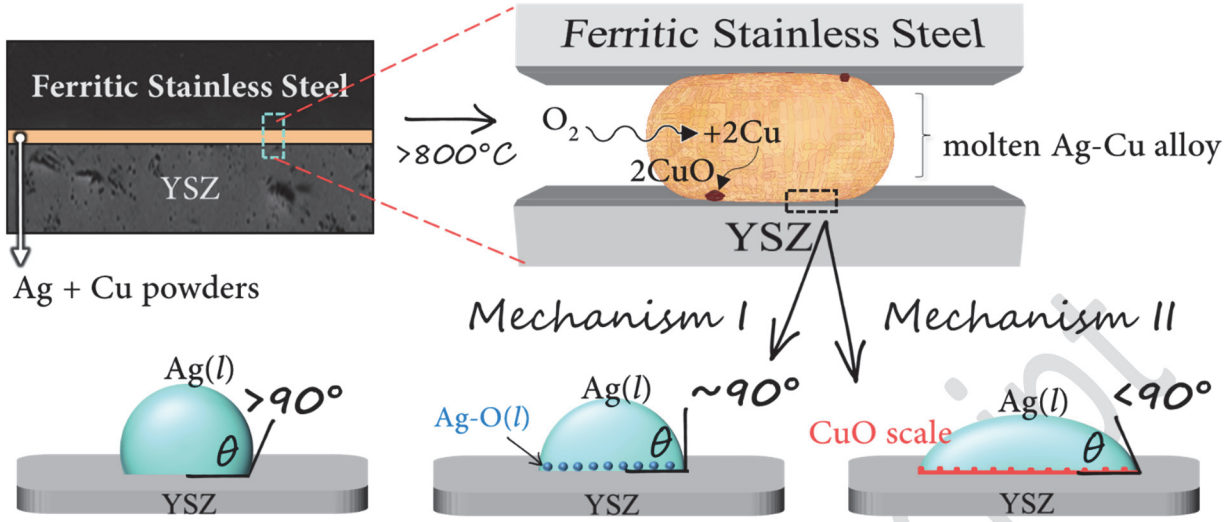


**Fig. 1.** Hypothetical mechanisms of how Ag-CuO braze enables wetting starting from the solid phase (left) to melting and wetting (right) during the heating process in air. While the wetting angle of Ag on YSZ > 90°, Ag-O clusters in Ag(*l*) solution may alter interfacial energy (*Mechanism I*), or addition of Cu may facilitate the formation of CuO interlayer on YSZ surface (*Mechanism II*) leading to a reduction of the wetting angle. The SEM images used for the representation of stainless steel and YSZ microstructure was taken from literature [24].

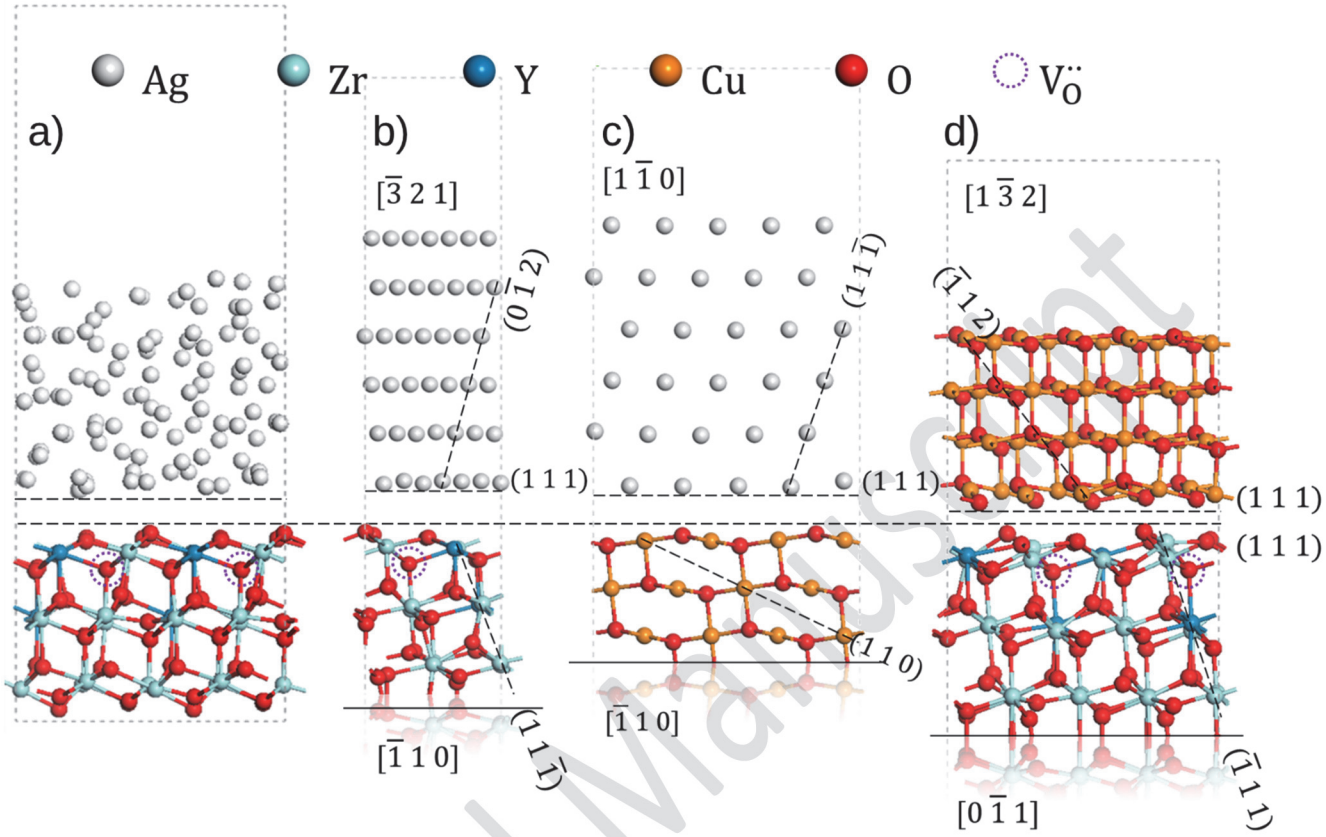


**Fig. 2.** Interfaces relaxed by PBE functional for investigation of Ag–CuO/YSZ braze. These include Ag(*l*)/YSZ (a), Ag/YSZ (b), Ag/CuO (c), and CuO/YSZ (d). Only the top half of the sandwich model of the solid-solid interface is shown due to symmetry.

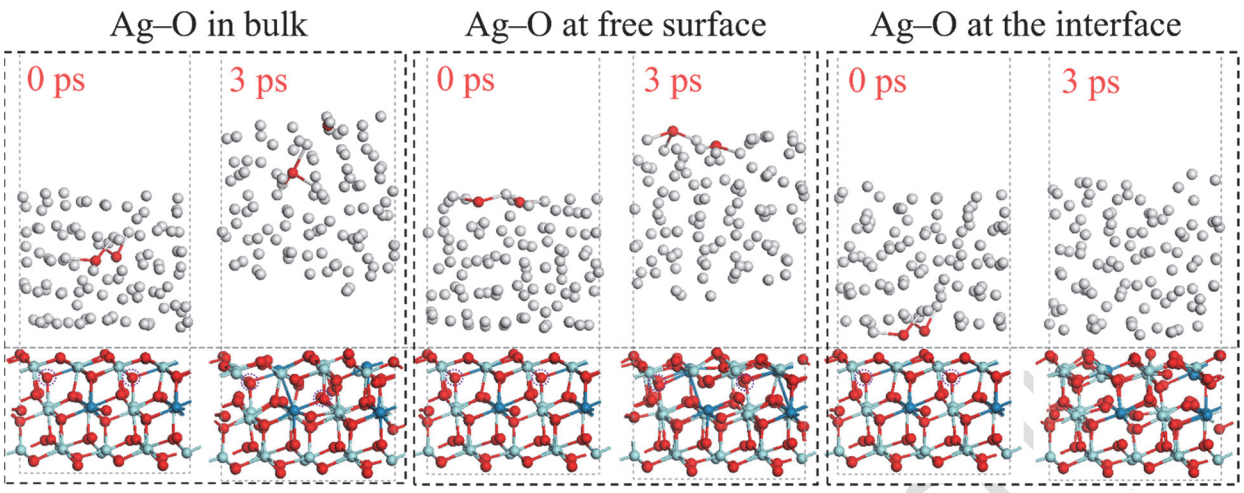


**Fig. 3.** Ag(*l*)/YSZ interface structures with dissolved oxygen atoms at the beginning and end of 3ps AIMD simulations at 1000 ˚C. Three initial positions of Ag–O clusters were investigated, including in the bulk Ag(*l*), at the free surface of Ag(*l*), and at the interface of Ag(*l*)/YSZ. The Ag-O at the interface is the most favorable structure.

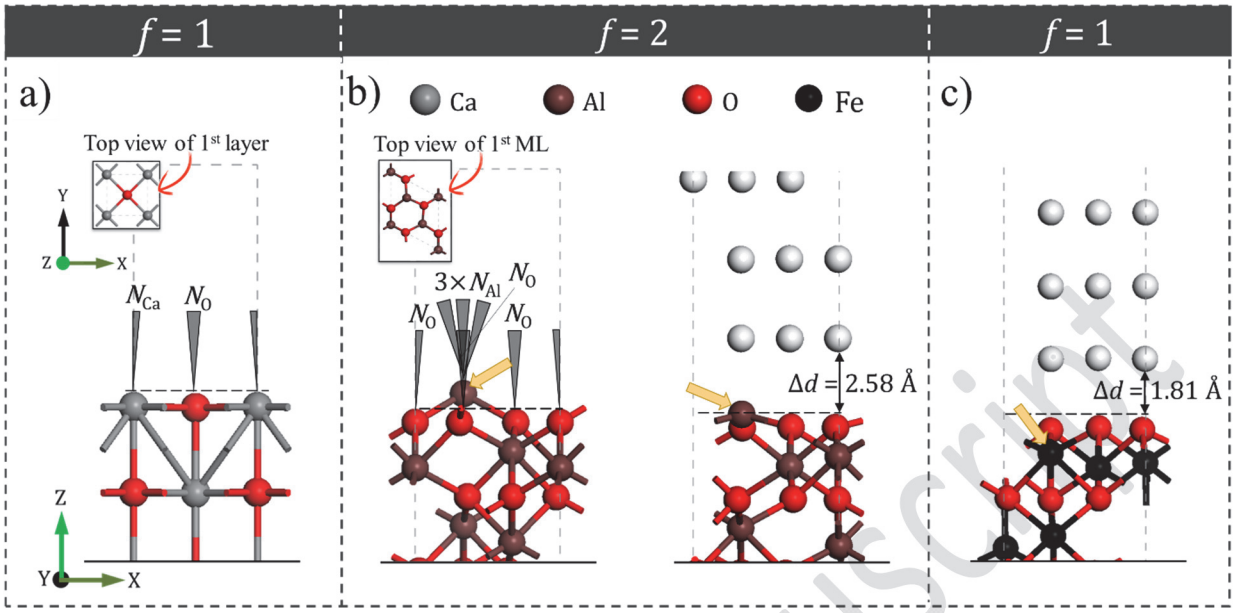


**Fig. 4.** Side view and top view of surface and interface structures to illustrate the formulation of the descriptor, $\chi_{MO}$, in Eqn 3. The $N_M$ and $N_O$ were demonstrated for a) an unrelaxed rock salt CaO {100} surface, where $f$=1 is used and b) an unrelaxed corundum oxide surface structure represented by the α-$Al_2O_3$ (0001). The relaxed interfaces of Ag/corundum-oxide demonstrate that b) in α-$Al_2O_3$ and other corundum-oxides $f$=2 is used as the protruded cation, $Al^{3+}$ , weakens Ag-O interfacial bonding, except c) in $Fe_2O_3$, whose cation, $Fe^{3+}$, submerges beneath the oxygen layer so it does not interfere the Ag-O bonds ($f$=1). The yellow arrows pinpoint the same cation in all the corundum oxides.

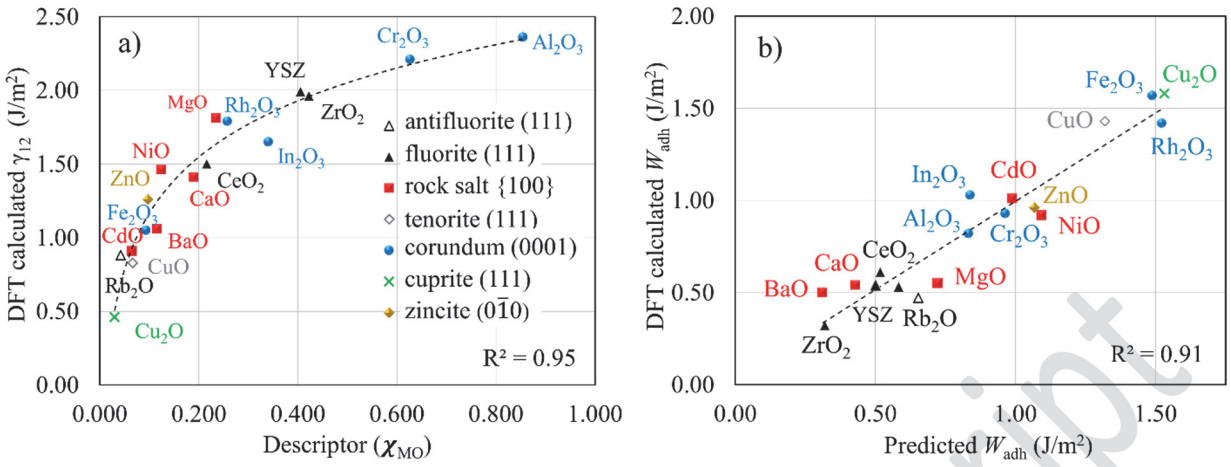


**Fig. 5.** The correlation a) between of the interface energy ($\gamma_{12}^{\mathrm{DFT}}$) of Ag/oxides and the descriptor ($\chi_{\mathrm{MO}}$), which followed a logarithmic function, and b) between the predicted work of adhesion ($W_{\mathrm{adh}}^{\mathrm{pred}}$) at Ag/oxides interface and the DFT calculated one ($W_{\mathrm{adh}}$).

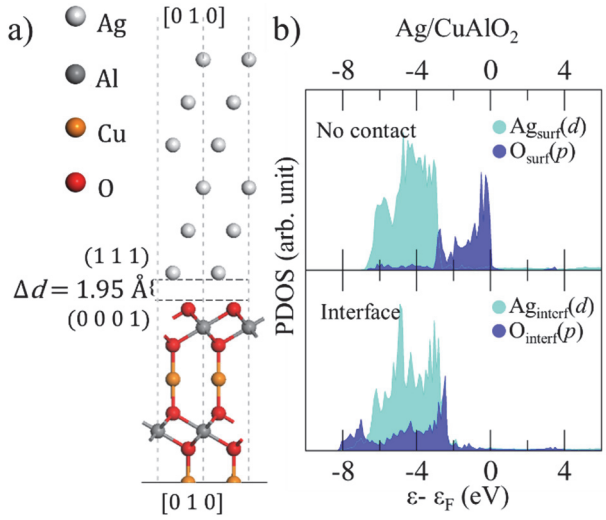


**Fig. 6.** The optimized structure of $Ag/CuAlO_2$ (half sandwich) by LDA functional showing an interface gap of 1.95 Å (a), and PDOS in the no-contact (10 Å apart) and interface positions (b).